Light: Science & Applications (2017) 6, e16192; doi:10.1038/lsa.2016.192
Official journal of the CIOMP 2047-7538/17
www.nature.com/lsa

ORIGINAL ARTICLE

Bragg-mirror-like circular dichroism in bio-inspired quadruple-gyroid 4srs nanostructures

Benjamin P Cumming[1,2], Gerd E Schröder-Turk[3], Sukanta Debbarma[4] and Min Gu[1,2]

The smooth and tailorable spectral response of Bragg mirrors has driven their pervasive use in optical systems requiring customizable spectral control of beam propagation. However, the simple nature of Bragg mirror reflection prevents their application to the control of important polarization states such as circular polarization. While helical and gyroid-based nanostructures exhibiting circular dichroism have been developed extensively to address this limitation, they are often restricted by the spectral inconsistency of their optical response. Here we present the fabrication and characterization of quadruple-gyroid 4srs nanostructures exhibiting bio-inspired Bragg-mirror-like circular dichroism: a smooth and uniform band of circular dichroism reminiscent of the spectrum of a simple multilayer Bragg-mirror. Furthermore, we demonstrate that the circular dichroism produced by 4srs nanostructures are robust to changes in incident angle and beam collimation, providing a new platform to create and engineer circular dichroism for functional circular polarization manipulation.
Light: Science & Applications (2017) **6,** e16192; doi:10.1038/lsa.2016.192; published online 13 January 2017

Keywords: Bio-inspired; Bragg-mirror; Chirality; Circular dichroism; Gyroid

INTRODUCTION

Bragg mirrors are essential building blocks of many optical systems due to their ability to achieve near-total reflection of light across a precisely defined band of wavelengths. Formed by the constructive interference of successive Fresnel reflections from within a simple multilayer dielectric stack[1,2], the reflection spectra of Bragg mirrors at normal incidence are characterized by a smooth, uniform and strong band of unpolarized reflection surrounded by high transmission[3]. Through these tailorable reflection properties, Bragg mirrors have found use in numerous applications requiring precise spectral control of beam propagation such as dielectric mirrors, beamsplitters and filters[4], fibre optic sensors and lasers[5], and in many other distributed feedback laser systems[6].

While the prevalence of devices facilitated by the reflection from Bragg mirrors is noteworthy, a growing demand to manipulate specific polarization states[7,8] has driven a focus on nanostructures capable of normal incidence interaction with a particular polarization. Specifically, a demand for control of spin angular momentum carrying circular polarization[8–10] has led to the development of chiral nanostructures such as helical spiral arrays[11–19] and gyroids[20–23] that exhibit circular dichroism: a differential reflection, transmission or absorption between left circularly polarized (LCP) and right circularly polarized (RCP) light. However, even though these structures can exhibit circular dichroism, their spectral behaviour is often dominated by sharp and narrow features[13–21], unpolarized reflection bands[16–18,22], and fluctuations in the sign of the circular dichroism[17–22] when a Bragg-mirror-like response, defined here as a spectral response comparable to the simple, clean and smooth spectrum of a Bragg mirror, would be preferred.

In this article we demonstrate the presence of bio-inspired Bragg-mirror-like (Bragg-like for short) circular dichroism in quadruple-gyroid **4srs** nanostructures that transmit only a single handedness of circular polarization. Taking inspiration from the strong but unpolarized Bragg-like reflections produced by the aligned single-gyroid **1srs**-based wing-scales of the butterfly *Parides sesostris*, we utilize the laser direct write technique to create and align new **4srs** nanostructures that exhibit smooth and strong circularly polarized transmission spectra reminiscent of the spectral response of a simple multilayer Bragg-mirror, and with similarities in its physical origin. We reveal a strong robustness of the circular dichroism band to variations in incident angle and beam collimation, and demonstrate the ability to incorporate defect modes within the circularly polarized stop-band that may enable the development of new chiral photonic devices.

MATERIALS AND METHODS

Crystallographic notation

Standard crystallographic notation with Miller indices is used to describe individual and families of directions and planes. The notations $<xyz>$ and $[xyz]$ are used to denote a family of directions equivalent by symmetry, and individual directions, respectively.

[1]Laboratory of Artificial-Intelligence Nanophotonics and CUDOS, School of Science, RMIT University, Melbourne, Victoria 3001, Australia; [2]Centre for Micro-Photonics, Faculty of Science, Engineering and Technology, Swinburne University of Technology, Hawthorn, Victoria 3122, Australia; [3]School of Engineering and Information Technology, Mathematics and Statistics, Murdoch University, Murdoch, Western Australia 6150, Australia and [4]Laser Physics Centre and CUDOS, Research School of Physical Sciences and Engineering, Australian National University, Canberra, Australian Capital Territory 2601, Australia
Correspondence: M Gu, Email: min.gu@rmit.edu.au
Received 5 April 2016; revised 11 July 2016; accepted 18 July 2016; accepted article preview online 21 July 2016

The notation (*xyz*) is used to denote an individual plane that is orthogonal to the direction [*xyz*].

Numerical simulations

Calculation of photonic band-structure modes is performed using the open source software package MPB, developed by MIT. The **4srs** and **1srs** nanostructures are constructed within simple cubic (SC) and body centred cubic (BCC) primitive unit cells, respectively, from cylindrical or elliptical line segments terminated by spherical and elliptical caps. Each nano-structure is discretized across the lattice vectors with a grid resolution of 64 pixels per lattice unit, and the dielectric function is averaged over a mesh size of 8 at each grid point. After solution of each frequency eigenvalue (ω), the corresponding magnetic eigenfield ($H^*_{k,n}$) with wave vector k is analysed for its degree of circular dichroism and for its coupling amplitude to a wave of arbitrary polarization[24,25]. To begin, the coupling amplitude between incident circularly polarized plane waves with wave vector $q \parallel k$ and the magnetic eigenfield in planes P orthogonal to k are computed via the overlap integrals

$$C^{\pm}_{k,n} = \left| \frac{1}{\iint_P dP} \iint_P \frac{1}{\sqrt{2}} (\hat{\mathbf{e}}_1 \pm i\hat{\mathbf{e}}_2) \cdot H^*_{k,n}(P) \right|^2 \quad (1)$$

where $\frac{1}{\sqrt{2}}(\hat{\mathbf{e}}_1 \pm i\hat{\mathbf{e}}_2)$ are the normalized circularly polarized plane waves and $H^*_{k,n}(P)$ is the normalized complex conjugate of the eigenfield in the plane P. The unit vectors $\hat{e}_1$ and $\hat{e}_2$ form an orthogonal set with k.

The degree of circular dichroism, C, which is termed the circular dichroism index, is given by the definition taken from the literature[24–27]

$$C_{k,n} = \mathrm{sgn}(q \cdot \nabla_k \omega) \left(\frac{C^+_{k,n} - C^-_{k,n}}{C^+_{k,n} + C^-_{k,n}} \right) \quad (2)$$

where sgn is the sign function. Similarly, the amplitude of coupling the mode to a wave of arbitrary polarization, β, which is termed the coupling index, is also given by the definition taken from the literature[24–27]

$$\beta_{k,n} = C^+_{k,n} + C^-_{k,n} \quad (3)$$

The circular dichroism and coupling indices are useful measures to quantify the nature of individual Bloch modes in terms of circular polarization, providing intuition for the full scattering problem that can only be solved when considering the complex band-structure including evanescent modes[28]. We consider 64 different planes along k within the magnetic eigenfield, averaging C and β across all the planes to reveal final mean values. The coupling index for each mode in the band diagrams is represented as the size of the plot while the circular dichroism index of each mode in the band-diagram is represented by the colour of the plot. Modes with $C < 0.5$ are considered LCP and are plotted blue, while modes with $C > 0.5$ are considered RCP and are plotted red. Modes with $\beta < 0.1$ are considered low-coupling modes.

Numerical simulations of the transmission spectra are performed using the commercial finite element software CST Microwave Studio. The cubic non-primitive unit-cell is used to model the **1srs** nanostructure transmission while the SC primitive unit-cell is used to model the **4srs** nanostructure. The $\alpha = 5°$ half apex angle illumination cone surrounding the [001] axis is modelled by a smoothed average of 95 plane wave simulations equally spaced over the cone of illumination.

Thick film deposition

Films of As_2S_3 of ≈16 μm thickness were prepared from stoichiometric As_2S_3 bulk glass using thermal evaporation[29]. A temperature controlled Ta baffled boat housing the As_2S_3 was held at a temperature of 310 °C in a vacuum chamber pumped to a base pressure of 2×10^{-7} torr. A carousel under planetary rotation at the top of the chamber held 170 μm thick glass substrates at room temperature and captured the evaporating As_2S_3 at a deposition rate of ≈ 0.6 nm s^{-1}. In the as-deposited state, the As_2S_3 films were measured to have an approximate refractive index of 2.35 that increases to 2.43 after annealing[30]. Raman spectroscopy was used to confirm that the deposited films contained the weakly interconnected As_4S_6 cage molecules that enable photo-polymerization[29,31]

Laser nano-fabrication

The full details of the adaptive optics enhanced direct laser writing system have been described elsewhere[22]. An amplified Ti:Sapphire femto-second laser, operating at a central wavelength of 800 nm, a repetition rate of 10 kHz and with a pulse duration of 100 fs is expanded to fill the area of a liquid crystal-based SLM (HSPDM5120785-PCIe, Boulder Nonlinear Systems) that provided phase-only modulation of the laser beam for compensating system-induced optical aberrations, as well as the strong spherical aberration that is imparted onto the beam when focusing through a glass coverslip and into the high refractive index As_2S_3. At this wavelength, the deposited film is transparent and no photo-polymerization occurs. Tracing the focus along the path of the **4srs** nets enables photo-polymerization back to As_2S_3 only of the **4srs** geometry and at any size and orientation that is desired. The use of adaptive optics in the fabrication system is essential to achieve high-quality nano-fabrication in As_2S_3 films as strong spherical aberration that is imparted onto the focused laser beam by the mismatch in glass and As_2S_3 refractive indices can significantly distort fabricated structures such as gyroids[22]. The reflected beam from the SLM was imaged to the back aperture of a high numerical aperture (NA = 1.4) objective lens that was used to focus the beam into the As_2S_3. A three-dimensional piezo-electric translation stage and mechanical shutter were used to translate the sample and switch the beam such that the focus of the laser traced out the network segments of the **4srs** within the As_2S_3 film. The **4srs** nanostructures were typically written at a speed of 10 μm s^{-1} and with an average laser power between 1.75 and 2.0 μW.

Wet chemical etching

After photo-polymerization, the As_2S_3 thick films were immersed for 3 min in a 2 mol-% ratio of diisopentylamine in dimethylsulfoxide at room temperature and with constant stirring. Immediately after etching, the films were immersed in acetone to cease the etching process.

Transmission spectroscopy

Transmission spectra were measured with a Fourier transform infrared spectrometer coupled to an infrared microscope. The microscope contained two Cassegrain reflection objectives for illumination and collection of transmitted light. Conversion of the broadband unpolarized light from the spectrometer to circular polarization was achieved via the addition of a broadband (2.5–10 μm) BaF_2 wire grid linear polarizer and a broadband (2.5–7 μm) MgF_2 circular polarizer. The incident beam was limited to a small cone of angles surrounding the [001] axis by placing a small aperture into the path of the objective lens, reducing the NA of the excitation from 0.68 NA to < 0.1 NA such that the beam extended over a cone with a half

doi:10.1038/lsa.2016.192

apex angle of $\alpha = 5°$. The measured spectra were corrected for measurement-induced spectral shifts and scattering losses, and smoothed to remove noise.

RESULTS AND DISCUSSION

4srs intergrowth

The **1srs** network (net) derives its name from the $SrSi_2$ crystal[32], within which the Si atoms form a single chiral network with cubic symmetry $I4_132$. Inflating the **1srs** net into cylindrical segments of finite radius forms a **1srs** nanostructure, also known as a single-gyroid, that is well suited to experimental fabrication[20–22]. A common unit-cell of the **1srs** nanostructure is the truncated octahedron with BCC basis[24,25,33,34], shown in Figure 1a. However, the only substantial circular dichroism within dielectric **1srs** nanostructures[24,25] is known to occur along the cubic <100> axes (see Materials and Methods for details of axes notation), often driving the use of a SC unit-cell[20–22] that aligns the four-screw single helices with the real-space lattice vectors, as shown in Figure 1b. It is the circular dichroism along these four-screw axes[24] that enables applications such as chiral beam-splitting[21], but with performance limited by a far from Bragg-like spectral response that includes sharp and narrow features, unpolarized reflection bands, as well as changes in the sign of circular dichroism[20–22].

For optimal control of circular polarization, it is desirable for a nanostructure to exhibit Bragg-like circular dichroism, characterized by simple reflection of an LCP (RCP) incident wave with a spectral response equivalent to that of a Bragg mirror, and simultaneous complete transmission of a RCP (LCP) incident wave. In complex 3D nanostructures, smooth Bragg-like reflections often exist along the primitive reciprocal directions of the lattice. For the **1srs** nanostructure, the primitive directions that are parallel to the <110> axes exhibit the broadest and cleanest Bragg-like band-gap (see Results and Discussion), a feature exploited by the butterfly *Parides sesostris*, which aligns the **1srs** <110> axes within specific patches of its wing-scales to maximize structural colouration[35]. The <110> axes of the **1srs** nanostructure, however, do not exhibit sensitivity to circular polarization[25] and new structures must be investigated if Bragg-like circular dichroism is to be exploited.

The quadruple-gyroid **4srs** net[24,32,36], which is comprised of four individual yet nonintersecting **1srs** nets of the same handedness, is a geometry that provides access to circularly polarized Bragg-like reflection bands by combining a SC primitive lattice type with cubic circular dichroism[24]. Building on the cubic symmetry of the **1srs** net, a **4srs** net is formed via simple half-lattice translations of three duplicate **1srs** nets—all of the same handedness—along each of the [100], [010] and [001] axes (Supplementary Fig. 1), ending in a **4srs** net such as the inflated nanostructure shown in Figure 1c. In this process, the four-screw single helices of the **1srs** are transformed into pairs of four-screw double helices[24], and a new SC primitive unit cell is formed with cubic symmetry $P4_232$, shown in Figure 1d. The length of the **4srs** primitive unit cell is half the length of the non-primitive cubic **1srs**

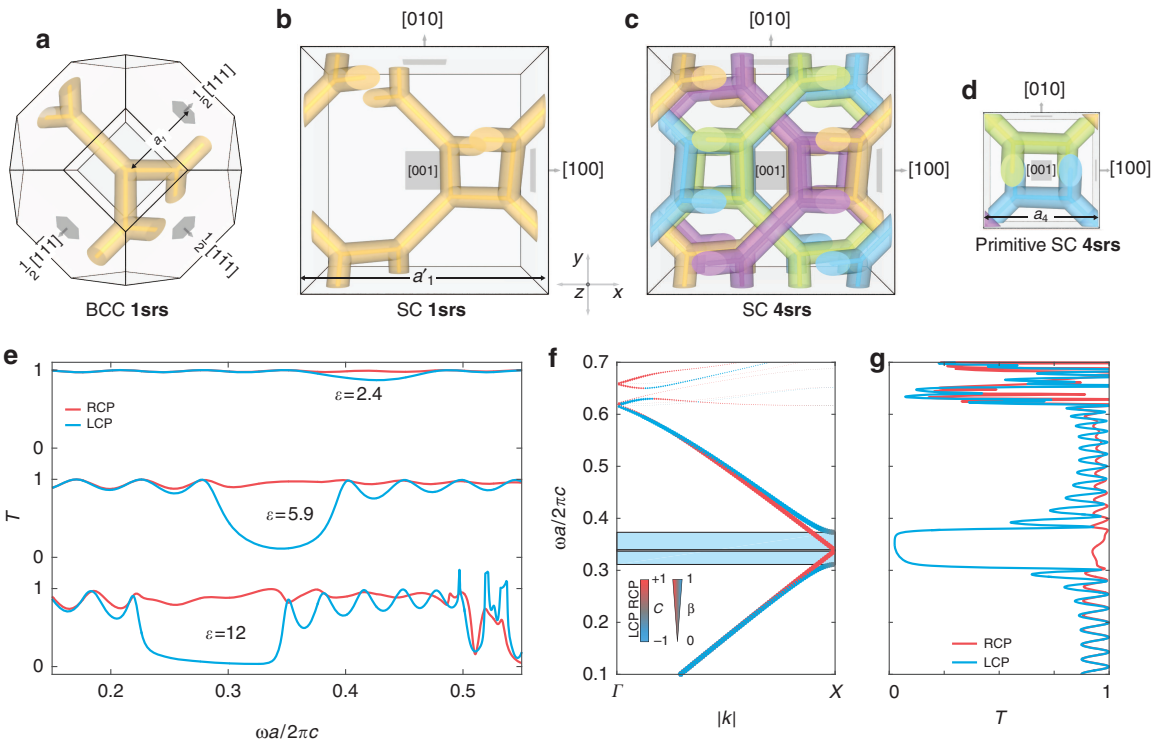

Figure 1 Geometry and numerical characterization of the quadruple-gyroid **4srs** nanostructure. (**a**) A BCC unit cell of a RHD **1srs** nanostructure (lattice parameter a_1). (**b**) A non-primitive cubic unit-cell of a RHD **1srs** nanostructure (lattice parameter a'_1) showing the four-screw helices along [001]. (**c**) A non-primitive cubic unit-cell of a RHD **4srs** nanostructure made of four identical **1srs** nanostructures. (**d**) A primitive SC unit-cell of a RHD **4srs** nanostructure (lattice parameter a_4) centred on the four-screw double helix. The grey patches and arrows indicate the direction of the real-space lattice vectors for each of the unit cells. (**e**) Simulated transmission spectra along the <100> axes for **4srs** nanostructures with a height of six unit cells, a volume fraction of $\Phi = 36\%$ and permittivities of $\varepsilon = 2.4$, $\varepsilon = 5.9$ and $\varepsilon = 12$. (**f**) Band-diagram (Γ–X) and (**g**) transmission spectra along the <100> axes for a RHD **4srs** nanostructure with $\varepsilon = 5.9$, $\Phi = 36\%$ and a height of 12 unit cells. The colour of the modes in *f* represents the mode's circular dichroism index, *C*, while the linewidth of the plot indicates the mode's coupling index, β (see Materials and Methods). The blue and grey shading indicates the location of the LCP stop-band, and narrow band-gap, respectively.

unit cell, even though the structural size of the four individual **1srs** nets remain the same, a result of the translation operation pair-wise exchanging the four network domains of the **4srs**.

Numerical simulations

The translation operations used to form the **4srs** nanostructure from a **1srs** nanostructure induce two important transformations in its optical behaviour. First, the transformation of the primitive real-space lattice type from BCC to SC shifts the primitive reciprocal lattice vectors parallel to the <100> axes (from parallel to the <110> axes), ensuring that the Bragg-like reflection often associated with the primitive reciprocal lattice directions (see Results and Discussion) will be in a cubic basis. Second, the transformation of the four-screw single helices of the **1srs** to the four-screw double helices of the **4srs** enhances sensitivity to circular polarized light[24] along the cubically symmetric <100> axes. Figure 1e illustrates the Bragg-like circular dichroism properties that result from the combination of these transformations, with numerically simulated LCP and RCP transmission spectra (see Materials and Methods) along the [100] axis of a right handed (RHD) **4srs** nanostructure plotted for the case of three relative **4srs** permittivities of $\varepsilon = 2.4$, $\varepsilon = 5.9$ and $\varepsilon = 12$ in a background of air ($\varepsilon = 1$), corresponding to the dielectric contrasts produced by common polymer[16,20,37], chalcogenide glass[22,29,31] and semiconductor[38–40] fabrication techniques, respectively.

To characterize the circular dichroism of each transmission spectrum plotted in Figure 1e, we define the strength of circular dichroism as the differential transmission between LCP and RCP incident waves: $\Delta T = T_{RCP} - T_{LCP}$, and define the width of the circular dichroism band as the gap to mid-gap ratio: $\Delta\omega = 2(\omega_2 - \omega_1)/(\omega_2 + \omega_1)$, where ω_1 and ω_2 are the upper and lower frequency bounds of the dichroism band, respectively. Low-permittivity materials produce only weak ($\Delta T = 11\%$) circular dichroism, limiting their practicality in experimental realization of the **4srs** nanostructure. Materials with larger permittivities such as typical semiconductors allow significantly strong and broad ($\Delta T = 92.5\%$, $\Delta\omega = 40\%$) circular dichroism bands to be opened, but at the cost of significant complexity in experimental realization[38–40]. Between these two extremes, chalcogenide glasses such as arsenic trisulfide (As_2S_3), which can be nanostructured in a similar manner to many low-permittivity polymers[22,29,31], can also open broad bands of circular dichroism ($\Delta T = 85.9\%$, $\Delta\omega = 22.9\%$) suitable for experimental realization.

As with previous simulations of topologically equivalent constant mean curvature **4srs** nanostructures[24], the origin of the dichroism band in the cylindrical **4srs** nanostructure is a splitting of the LCP and RCP mode frequencies surrounding the narrow band-gap along the <100> axes[24]. Figure 1f shows the numerically simulated band-structure (see Materials and Methods) along the <100> axes for a cylindrical RHD As_2S_3 **4srs** geometry with a dielectric volume fraction (Φ) of 36%, and is plotted alongside a simulation of the transmission spectra in Figure 1g for incident waves propagating through the same geometry. Each mode in the band-diagram in Figure 1f is analysed for its degree of circular dichroism and coupling amplitude (see Materials and Methods), plotted as the colour and linewidths of the curve, respectively. A clear separation of the first four LCP and RCP modes at the X point is evident, opening a LCP stop-band to create a band of circular dichroism 2.5 times wider than that produced by an equivalent RHD As_2S_3 **1srs** nanostructure (Supplementary Fig. 2). A full band-structure analysis of the **4srs** nanostructure can be found in Supplementary Fig. 3, highlighting the unique Bragg-like circular dichroism properties of the cubic <100> axes.

Laser nano-fabrication of 4srs nanostructures

Unlike the **1srs** geometry that is found ubiquitously in nature[32] and which has been experimentally realized by means of self-assembly[37,41,42], bio-templating[43,44], laser direct write techniques[20–22] and 3D printing[45], no **4srs** nanostructures have been either found or produced, although the occurrence of various triply intergrown geometries[46–49] raises the hope that a self-assembly strategy for the **4srs** will eventually be found. To experimentally realize the **4srs** nanostructure for the first time, we utilized the laser direct write technique in the chalcogenide glass As_2S_3 to create cylindrical As_2S_3 **4srs** nanostructures in a three-step process as detailed in Figure 2a–2c

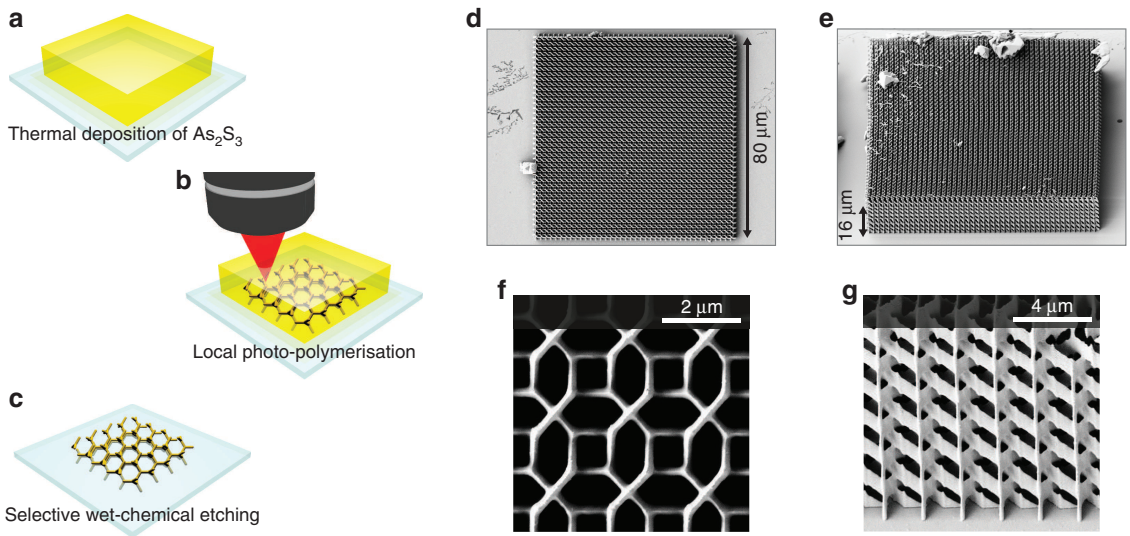

Figure 2 Three-step fabrication process of the As_2S_3 laser direct write technique and fabricated As_2S_3 **4srs** nanostructures. (**a**) Thermal deposition of As_2S_3 glass. (**b**) Local photo-polymerization with a focused femto-second laser beam, and (**c**) selective wet-chemical etching to reveal a free-standing nanostructure. (**d**) SEM image of a fabricated RHD **4srs** nanostructure along the [001] axis. (**e**) SEM image of a fabricated RHD **4srs** nanostructure along the [011] axis. (**f**, **g**) are close-up images of the views in (**d**) and (**e**) showing the geometry of the four-screw double helices.

doi:10.1038/lsa.2016.192

and described in the Materials and Methods section. First, thick films of As_2S_3 were deposited onto glass substrates using a controlled deposition procedure that preferentially deposits the As_2S_3 as weakly interconnected As_4S_6 cage molecules[29,31]. Second, the as-deposited films were locally and three-dimensionally photo-polymerized back to cross-linked As_2S_3 with an adaptive optics enhanced direct laser writing system[22]. Third, the films were wet-chemically etched to enable preferential dissolution of the unexposed As_4S_6, leaving a free-standing As_2S_3 nano-structure with high dielectric contrast to the surrounding air.

Using this technique, **4srs** nanostructures with primitive lattice parameters between $a_4 = 1.75$ and 2 μm were fabricated with line-widths between 150 and 240 nm along the [100] and [010] axes, and between 0.9 and 1.2 μm along the [001] axis, such that volume fractions covering the optimal value of $\Phi = 19\%$ (Supplementary Fig. 4h) were produced. In all cases, the nanostructures were oriented such that the [001] axis was perpendicular to the substrate surface and access to the four-screw double helices was possible.

Scanning electron microscope (SEM) images of fabricated **4srs** nanostructures along the [001] and [011] axes are shown in Figure 2d and 2e, with additional close-up images shown in Figure 2f and 2g showing the characteristic four-screw double helices that separate the band-edge mode frequencies[24] and lead to the opening of a circular dichroism band. The angled images along the [011] axis reveal a large degree of elongation of the network linewidth along the [001] axis. This elongation is the result of the elliptical shape of the diffraction limited focus in most laser writing systems, which for the system used here directly transforms the symmetric cylindrical segments of the **4srs** to elliptic cylindrical segments with an ellipticity of $e = 5$, where e is defined by the ratio of the [001] to [100] lines widths of the elliptical line segments. Such elongation breaks the cubic symmetry of the **4srs** nanostructure, and a variety of methods have been developed in order to restore it[21,22,31]. However, as long as symmetry is maintained in the plane orthogonal to the [001] axis, the ellipticity will have negligible effect on the circular dichroism bands along the [001] axis (Supplementary Fig. 4) and hence preservation of cubic symmetry is not always necessary.

Transmission spectroscopy of 4srs nanostructures

To probe the circular dichroism of the **4srs** nanostructures, Fourier transform infrared spectroscopy (see Materials and methods) was utilized to measure the circularly polarized transmission spectra across the mid-infrared wavelength range. The etched networks were mounted in the spectrometer such that the incident beam propagated parallel to the [001] axis, while the incident angle was limited to a narrow cone with a half apex angle (α) of 5° as shown in the measurement geometry in Figure 3a and 3b. Figure 3c and 3d shows the measured and simulated **4srs** transmission spectra, respectively, for both LCP and RCP incident waves traversing a RHD **4srs** nanostructure with $a_4 = 2$ μm and lateral and axial linewidths of 235 and 1,175 nm, respectively, corresponding to a volume fraction of $\Phi = 17.7\%$. A strong reduction in transmission for the LCP incident beam is observed compared with the case of a RCP incident beam that propagates unaffected by the structure, resulting in the opening of a broad ($\Delta\omega = 18\%$) and strong ($\Delta T = 65\%$) band of Bragg-like circular dichroism. In comparison, the measured and simulated transmission

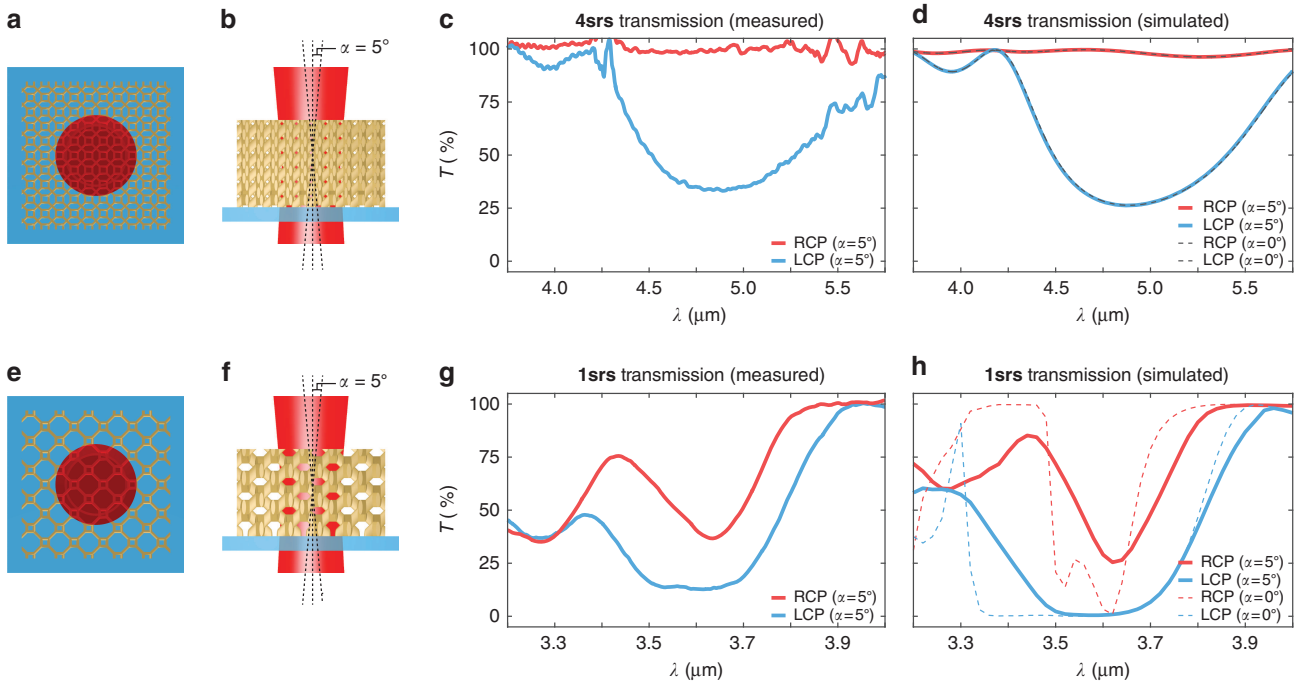

Figure 3 Experimental transmission characterization of the robust **4srs** nanostructure circular dichroism and comparison with numerical simulations. (**a**, **b**) Transmission measurement geometry for the **4srs** nanostructure. (**c**) Measured transmission spectra for a RHD **4srs** nanostructure with a lattice parameter of $a_4 = 2$ μm, a height of six unit cells, a lateral linewidth of 235 nm and $e = 5$. (**d**) Simulated transmission spectra at normal incidence ($\alpha = 0°$) (dotted black lines) and at $\alpha = 5°$ (solid coloured lines) for a **4srs** geometry equivalent to the experimental measurement. (**e**, **f**) Transmission measurement geometry for the **1srs** nanostructure. (**g**) Measured transmission spectra for a RHD **1srs** nanostructure with a lattice parameter $a_1' = 3$ μm, a height of four unit cells, a lateral linewidth of 205 nm and $e = 5$. (**h**) Simulated transmission spectra at normal incidence ($\alpha = 0°$) (dashed thin lines) and at $\alpha = 5°$ (solid thick lines) for a **1srs** geometry equivalent to the experimental measurement.

spectra for LCP and RCP incident waves traversing the [001] axis (Figure 3e and 3f) of a **1srs** nanostructure (see Supplementary Fig. 5 for SEM images) can be seen in Figure 3g and 3h, respectively, where two considerably narrower bands of circular dichroism with a maximum width of $\Delta\omega = 5.6\%$ exist in a significantly more complex transmission spectra that includes dips in transmission for both left- and right-handed circularly polarized waves.

In addition to the presence of strong and broadband circular dichroism, comparison between the measured and simulated transmission spectra reveals a further advantage of the **4srs** nanostructure over similar **1srs** nanostructures. For the case of the **4srs** nanostructure, good agreement is found between the measured and transmission spectra when accounting for both the full $\alpha = 5°$ half apex angle of the incident beam, as well as when the simulation is limited to normal incidence ($\alpha = 0°$). The **1srs** nanostructure however, shows significant deviation between the numerical simulations at normal incidence and at $\alpha = 5°$. This indicates excellent robustness of the **4srs** nanostructure to changes in both the incident angle, and to deviations from plane wave illumination surrounding the [001] axis.

The origin of the Bragg-like characteristics of the circular dichroism band lies in the coincidence of the four-screw double-helix axes with the direction of the primitive reciprocal lattice vectors. Along these primitive directions, the first Brillouin zone is met with the shortest possible wave-vectors such that other reciprocal lattice vectors that possess much larger wave-vector lengths cannot contribute to the band structure. In such a situation, the scattering problem reduces approximately to a single-mode problem equivalent to the situation of a Bragg mirror or simple multilayer stack[25] and accordingly, a simple band-gap with strong reflection is surrounded by a single pair of modes permitting high transmission is opened. In combination with the distinct topological continuities of opposite handed screw motions along the four-screw double helices[24,25] that drive a large separation of LCP and RCP mode frequencies, the band-gap is transformed into a broad band of circular dichroism with a spectral response reminiscent of the clean broadband reflection from a Bragg mirror.

The origin of the robustness to incident angle arises from the SC symmetry of the **4srs**, which translates to a SC Brillouin zone in reciprocal space, shown in Figure 4a and 4b. Real-space propagation along the <100> axes corresponds to wave-vectors, **k**, terminating at the face of the Brillouin zone, such that small changes to the incident angle, θ, increase $|k|$ in quadratic order. Accordingly, the band-edge mode frequencies undergo only a minor blue-shift as shown in Figure 4c, which plots the spectral position of the circular dichroism band for the experimental **4srs** geometry as a function of θ. In contrast, the **1srs** has BCC symmetry regardless of the choice of experimentally convenient non-primitive cubic unit cell, resulting in a face centred cubic (FCC) Brillouin zone in reciprocal space, shown in Figure 4d and 4e. In this case, real-space propagation along the <100> axes corresponds to wave-vectors that terminate at the Brillouin zone four-edge vertices, such that a small change in the incident angle result in a large decrease in $|k|$. Consequently, the band-edge mode frequencies undergo a strong red-shift as shown in Figure 4f, which plots the spectral position of the experimental **1srs** circular dichroism bands (see Supplementary Fig. 6 for a band-diagram of this geometry) as a function of θ. For small angles of incidence, the disparate shift in mode frequencies between the two networks is present for all volume fractions and network ellipticities, as shown in Supplementary Fig. 7. This indicates that the switch from BCC to SC symmetry can provide robustness to angle of incidence in the presence of the most common geometric variations, so long as the topology of the network is preserved.

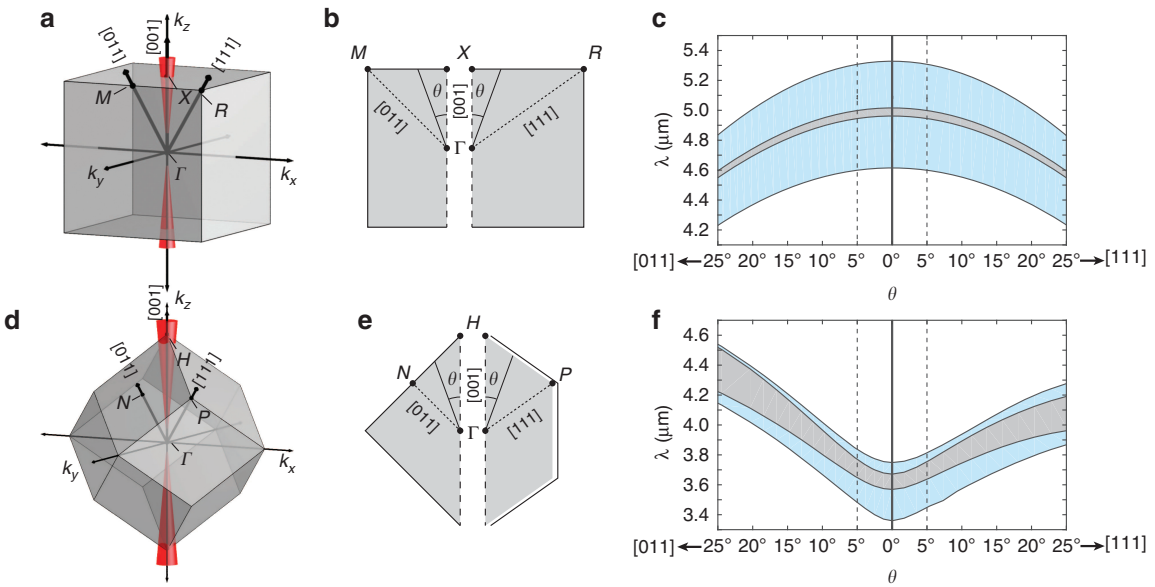

Figure 4 Origin of the robust circular dichroism in quadruple-gyroid **4srs** nanostructures. (**a**) First Brillouin zone of a **4srs** nanostructure and the measured wave-vectors (red cone) within the $\alpha = 5°$ half apex angle around [001]. (**b**) Partial cross-sections of the *Γ–X–M* and *Γ–X–R* Brillouin zone planes for the **4srs** nanostructure. (**c**) Plot of the **4srs** nanostructure circular dichroism bands (blue shading) and band-gap (grey shading) spectral positions as a function of incident angle (θ) from [001] to [011] and [111]. (**d**) First Brillouin zone of the **1srs** nanostructure and the measured wave-vectors (red cone) within the $\alpha = 5°$ half apex angle around [001]. (**e**) Partial cross-sections of the *Γ–H–N* and *Γ–H–P* Brillouin zone planes for the **1srs** nanostructure. (**f**) Plot of the **1srs** nanostructure circular dichroism band spectral position as a function of incident angle (θ) from [001] to both [011] and [111].

doi:10.1038/lsa.2016.192

One possible application of the **4srs** nanostructure is in the engineering of defect states[50,51] within the circular dichroism band. In particular, quarter-twist planar defect layers[52,53] can introduce a defect mode precisely at the mid-gap wavelength of a circular dichroism band[52,53]. Supplementary Fig. 8 shows transmission spectra and SEM images of a fabricated RHD **4srs** nanostructure with a quarter-twist defect layer in the (001) plane, creating a single defect mode within the circular dichroism band and producing a peak in LCP transmission that is pinned to the mid-gap wavelength. Such defects may be useful for tailoring the position and strength of circular dichroism bands[52], or increasing the photonic density of states for chiral lasing[51].

CONCLUSION

We have shown that the quadruple-gyroid **4srs** nanostructure is a remarkable nanostructure that provides an exceptional ability to filter broad bands of circularly polarized light with strong resilience against deviations in the angle of incidence and beam collimation, even when the nanostructure possesses asymmetric cylindrical segments. Furthermore, we have shown that the **4srs** nanostructure allows for the creation of Bragg-like circular dichroism without spectral inconsistencies, unlike many other chiral structures that exhibit non-uniform circular dichroism and transmission[13–22].

CONFLICT OF INTEREST

The authors declare no conflict of interest.

ACKNOWLEDGEMENTS

This research was conducted by the Australian Research Council Centre of Excellence for Ultrahigh bandwidth Devices for Optical Systems (project number CE110001018). We would like to thank Matthias Saba, Johannes Hielscher and Mark D. Turner for their useful discussions on the numerical simulations and experimental fabrication.

1 Rayleigh L. On the maintenance of vibrations by forces of double frequency, and on the propagation of waves through a medium endowed with a periodic structure. *Phil Mag Ser 5* 1887; **24**: 145–159.
2 Joannopoulos JD, Johnson SG, Winn JN, Meade RD. *Photonic Crystals: Molding the Flow of Light*, 2nd edn Princeton University Press: Princeton. 2011.
3 Gong QH, Hu XY. *Photonic Crystals: Principles and Applications*. Pan Stanford Publishing: Stanford. 2014.
4 MacLeod HA, Macleod HA. *Thin-Film Optical Filters*, 4th edn. CRC Press: New York. 2010.
5 Kashyap R. *Fiber Bragg Gratings*. Academic Press: New York. 2010.
6 Carroll JE, Whiteaway J, Plumb D. *Distributed Feedback Semiconductor Lasers*. Institution of Electrical Engineers: London. 1998.
7 Noda S, Yokoyama M, Imada M, Chutinan A, Mochizuki M. Polarization mode control of two-dimensional photonic crystal laser by unit cell structure design. *Science* 2001; **293**: 1123–1125.
8 O'Brien JL, Furusawa A, Vučković J. Photonic quantum technologies. *Nat Photon.* 2009; **3**: 687–695.
9 Bozinovic N, Yue Y, Ren YX, Tur M, Kristensen P *et al*. Terabit-scale orbital angular momentum mode division multiplexing in fibers. *Science* 2013; **340**: 1545–1548.
10 D'Ambrosio V, Nagali E, Walborn SP, Aolita L, Slussarenko S *et al*. Complete experimental toolbox for alignment-free quantum communication. *Nat Commun* 2012; **3**: 961.
11 Gansel JK, Thiel M, Rill MS, Decker M, Bade K *et al*. Gold helix photonic metamaterial as broadband circular polarizer. *Science* 2009; **325**: 1513–1515.
12 Yang ZY, Zhao M, Lu PX. Improving the signal-to-noise ratio for circular polarizers consisting of helical metamaterials. *Opt Express* 2011; **19**: 4255–4260.
13 Radke A, Gissibl T, Klotzbücher T, Braun PV, Giessen H. Three-dimensional bichiral plasmonic crystals fabricated by direct laser writing and electroless silver plating. *Adv Mater* 2011; **23**: 3018–3021.
14 Kaschke J, Wegener M. Gold triple-helix mid-infrared metamaterial by STED-inspired laser lithography. *Opt Lett* 2015; **40**: 3986–3989.
15 Thiel M, Hermatschweiler M, Wegener M, von Freymann G. Thin-film polarizer based on a one-dimensional–three-dimensional–one-dimensional photonic crystal heterostructure. *Appl Phys Lett* 2007; **91**: 123515.
16 Thiel M, Decker M, Deubel M, Wegener M, Linden S *et al*. Polarization stop bands in chiral polymeric three-dimensional photonic crystals. *Adv Mater* 2007; **19**: 207–210.
17 Thiel M, Rill MS, von Freymann G, Wegener M. Three-dimensional bi-chiral photonic crystals. *Adv Mater* 2009; **21**: 4680–4682.
18 Thiel M, Fischer H, von Freymann G, Wegener M. Three-dimensional chiral photonic superlattices. *Opt Lett* 2010; **35**: 166–168.
19 Kao T-H, Chien L-YC, Hung Y-C. Dual circular polarization gaps in helix photonic metamaterials. *Opt Express* 2015; **23**: 24416–24425.
20 Turner MD, Schröder-Turk GE, Gu M. Fabrication and characterization of three-dimensional biomimetic chiral composites. *Opt Express* 2011; **19**: 10001–10008.
21 Turner MD, Saba M, Zhang QM, Cumming BP, Schröder-Turk GE *et al*. Miniature chiral beamsplitter based on gyroid photonic crystals. *Nat Photon.* 2013; **7**: 801–805.
22 Cumming BP, Turner MD, Schröder-Turk GE, Debbarma S, Luther-Davies B *et al*. Adaptive optics enhanced direct laser writing of high refractive index gyroid photonic crystals in chalcogenide glass. *Opt Express* 2014; **22**: 689–698.
23 Dolan JA, Wilts BD, Vignolini S, Baumberg JJ, Steiner U *et al*. Optical properties of gyroid structured materials: from photonic crystals to metamaterials. *Adv Opt Mater* 2015; **3**: 12–32.
24 Saba M, Thiel M, Turner MD, Hyde ST, Gu M *et al*. Circular dichroism in biological photonic crystals and cubic chiral nets. *Phys Rev Lett* 2011; **106**: 103902.
25 Saba M, Wilts BD, Hielscher J, Schröder-Turk GE. Absence of circular polarisation in reflections of butterfly wing scales with chiral gyroid structure. *Mater Today* 2014; **1**: 193–208.
26 Lee JCW, Chan CT. Polarization gaps in spiral photonic crystals. *Opt Express* 2005; **13**: 8083–8088.
27 Oh SS, Demetriadou A, Wuestner S, Hess O. On the origin of chirality in nanoplasmonic gyroid metamaterials. *Adv Mater* 2013; **25**: 612–617.
28 Saba M, Schröder-Turk GE. Bloch modes and evanescent modes of photonic crystals: weak form solutions based on accurate interface triangulation. *Crystals* 2015; **5**: 14–44.
29 Nicoletti E, Zhou GY, Jia BH, Ventura MJ, Bulla D *et al*. Observation of multiple higher-order stopgaps from three-dimensional chalcogenide glass photonic crystals. *Opt Lett* 2008; **33**: 2311–2313.
30 Choi D-Y, Madden S, Bulla D, Wang RP, Rode A *et al*. Thermal annealing of arsenic trisulphide thin film and its influence on device performance. *J Appl Phys* 2010; **107**: 053106.
31 Wong S, Deubel M, Pérez-Willard F, John S, Ozin GA *et al*. Direct laser writing of three-dimensional photonic crystals with a complete photonic bandgap in chalcogenide glasses. *Adv Mater* 2006; **18**: 265–269.
32 Hyde ST, O'Keeffe M, Proserpio DM. A short history of an elusive yet ubiquitous structure in chemistry, materials, and mathematics. *Angew Chem Int Ed Engl* 2008; **47**: 7996–8000.
33 Lu L, Fu L, Joannopoulos JD, Soljačić M. Weyl points and line nodes in gyroid photonic crystals. *Nat Photon.* 2013; **7**: 294–299.
34 Lu L, Wang ZY, Ye DX, Ran LX, Fu L *et al*. Experimental observation of Weyl points. *Science* 2015; **349**: 622–624.
35 Yoshioka S, Fujita H, Kinoshita S, Matsuhana B. Alignment of crystal orientations of the multi-domain photonic crystals in Parides sesostris wing scales. *J R Soc Interface* 2013; **11**: 20131029.
36 Wells AF. *Three Dimensional Nets and Polyhedra*. Wiley: New York. 1977.
37 Urbas AM, Maldovan M, DeRege P, Thomas EL. Bicontinuous cubic block copolymer photonic crystals. *Adv Mater* 2002; **14**: 1850–1853.
38 Hermatschweiler M, Ledermann A, Ozin GA, Wegener M, von Freymann G. Fabrication of silicon inverse woodpile photonic crystals. *Adv Funct Mater* 2007; **17**: 2273–2277.
39 Tétreault N, von Freymann G, Deubel M, Hermatschweiler M, Pérez-Willard F *et al*. New route to three-dimensional photonic bandgap materials: Silicon double inversion of polymer templates. *Adv Mater* 2006; **18**: 457–460.
40 García-Santamaría F, Xu M, Lousse V, Fan S, Braun PV *et al*. A germanium inverse woodpile structure with a large photonic band gap. *Adv Mater* 2007; **19**: 1567–1570.
41 Chan VZ-H Hoffman J, Lee VY, Iatrou H, Avgeropoulos A *et al*. Ordered bicontinuous nanoporous and nanorelief ceramic films from self assembling polymer precursors. *Science* 1999; **286**: 1716–1719.
42 Hajduk DA, Harper PE, Gruner SM, Honeker CC, Kim G *et al*. The gyroid: a new equilibrium morphology in weakly segregated diblock copolymers. *Macromolecules* 1994; **27**: 4063–4075.
43 Mille C, Tyrode EC, Corkery RW. 3D titania photonic crystals replicated from gyroid structures in butterfly wing scales: approaching full band gaps at visible wavelengths. *RSC Adv* 2013; **3**: 3109–3117.
44 Mille C, Tyrode EC, Corkery RW. Inorganic chiral 3-D photonic crystals with bicontinuous gyroid structure replicated from butterfly wing scales. *Chem Commun* 2011; **47**: 9873–9875.
45 Pouya C, Vukusic P. Electromagnetic characterization of millimetre-scale replicas of the gyroid photonic crystal found in the butterfly *Parides sesostris*. *Interface Focus* 2012; **2**: 645–650.
46 Fischer MG, de Campo L, Kirkensgaard JJK, Hyde ST, Schröder-Turk GE. The tricontinuous 3*ths*(5) phase: a new morphology in copolymer melts. *Macromolecules* 2014; **47**: 7424–7430.
47 Han Y, Zhang DL, Chng LL, Sun JL, Zhao L *et al*. A tri-continuous mesoporous material with a silica pore wall following a hexagonal minimal surface. *Nat Chem* 2009; **1**: 123–127.

48 Sorenson GP, Schmitt AK, Mahanthappa MK. Discovery of a tetracontinuous, aqueous lyotropic network phase with unusual 3D-hexagonal symmetry. *Soft Matter* 2014; **10**: 8229–8235.
49 Schroder-Turk GE, de Campo L, Evans ME, Saba M, Kapfer SC *et al.* Polycontinuous geometries for inverse lipid phases with more than two aqueous network domains. *Faraday Discuss* 2013; **161**: 215–247.
50 Braun PV, Rinne SA, García-Santamaría F. Introducing defects in 3D photonic crystals: state of the art. *Adv Mater* 2006; **18**: 2665–2678.
51 Kopp VI, Zhang ZQ, Genack AZ. Lasing in chiral photonic structures. *Prog Quant Electron* 2003; **27**: 369–416.
52 Hodgkinson IJ, Wu QH, Thorn KE, Lakhtakia A, McCall MW. Spacerless circular-polarization spectral-hole filters using chiral sculptured thin films: theory and experiment. *Opt Commun* 2000; **184**: 57–66.
53 Kopp VI, Genack AZ. Twist defect in chiral photonic structures. *Phys Rev Lett* 2002; **89**: 033901.

This work is licensed under a Creative Commons Attribution-NonCommercial-NoDerivs 4.0 International License. The images or other third party material in this article are included in the article's Creative Commons license, unless indicated otherwise in the credit line; if the material is not included under the Creative Commons license, users will need to obtain permission from the license holder to reproduce the material. To view a copy of this license, visit http://creativecommons.org/licenses/by-nc-nd/4.0/

© The Author(s) 2017

Supplementary Information for this article can be found on the *Light: Science & Applications*' website (http://www.nature.com/lsa).